

Benchmarking of a high-fidelity mixed-species entangling gate

A. C. Hughes,[†] V. M. Schäfer,^{†,*} K. Thirumalai,[†] D. P. Nadlinger, S. R. Woodrow, D. M. Lucas, and C. J. Ballance

Department of Atomic and Laser Physics, University of Oxford

(Dated: June 18, 2022)

Logic gates between different species of qubit are a powerful resource for quantum computing, networking, clocks, and spectroscopy. We implement a two-qubit gate between a $^{43}\text{Ca}^+$ hyperfine qubit and a $^{88}\text{Sr}^+$ Zeeman qubit. For this pair of ion species, the S-P optical transitions are close enough that a single laser of wavelength 402 nm can be used to drive the gate, but sufficiently well separated to give good spectral isolation and low photon scattering errors. We characterize the gate by full randomized benchmarking, gate set tomography and Bell state analysis. The latter method gives a fidelity of 99.8(1)%, comparable to that of the best same-species gates.

The exchange of quantum information between different types of qubit is a powerful tool for a wide variety of applications: these range from quantum computing and networking, to optical clocks, to spectroscopy of molecules or exotic species for testing fundamental physics. In quantum information processing (QIP), interfacing different systems allows the use of specialized qubits for different operations (for example, memory, logic and readout) [1, 2], coupling of matter and photonic qubits for communication or distributed computing [3–9], and even the connection of distinct qubit platforms (such as solid state and atomic systems [10–12]). While incoherent quantum state transfer is often sufficient for spectroscopy or clocks [13–17], general QIP requires two-qubit interactions that preserve phase and amplitude of superposition states, i.e. entangling gate operations.

Trapped-ion systems are an extremely promising technology for QIP, further enriched by the diversity of atomic properties of different species. The use of two spectrally-resolved species allows laser cooling, state preparation and readout via one species without corrupting logic qubits held in the second species [18, 19]. Different species also facilitate networking, where ions whose level structures and transition wavelengths are well suited to photonic interfacing can be gated with ions possessing superior properties for logic or memory [6, 20]. Both mixed-isotope and mixed-element two-qubit gates have previously been demonstrated [20–25]. However, due to the extra technical complications of dual-species setups and new sources of error to which multi-species gates are susceptible, the gate fidelities achieved have fallen short of the state-of-the-art for single-species gates [26–30].

In this work, we perform a mixed-element $\sigma_z \otimes \sigma_z$ geometric phase gate [31] between $^{43}\text{Ca}^+$ and $^{88}\text{Sr}^+$, where the ions are driven by a state-dependent force tuned close to resonance with a motional mode. We take advantage of the extremely low addressing errors ($< 10^{-6}$) of qubits with different energy splittings to characterize the gate performance using randomized benchmarking (RBM) with full exploration of the two-qubit Hilbert space, by gate set tomography (GST), and by partial Bell state tomography (PST).

Calcium and strontium are a particularly well-

matched pair of elements: they have S-P transitions at (393, 397) nm and (408, 422) nm respectively, the closest of which are only 20 THz apart (Fig.1a). This frequency separation is small enough that a single Raman laser of modest intensity, at around 402 nm, can provide a state-dependent force on both species simultaneously to perform a two-qubit gate, but large enough to give small ($\sim 10^{-4}$) photon scattering errors during the gate, and to preserve excellent spectral isolation during cooling and readout [32, 33]. The Raman beatnote required to drive a $\sigma_z \otimes \sigma_z$ gate depends only on the motional mode frequency f_{mot} and is independent of the qubit frequency. Therefore a single pair of Raman beams can perform a gate between $^{88}\text{Sr}^+$ and $^{43}\text{Ca}^+$ ions, similarly to the gate previously performed on two different isotopes of calcium [21]. This simplifies the technical setup compared with previous demonstrations of mixed-element logic gates, which required separate laser systems for each species [20, 22]. The masses of $^{43}\text{Ca}^+$ and $^{88}\text{Sr}^+$ differ only by a factor of two, yielding sufficient motional coupling for efficient sympathetic cooling [34, 35]. $^{43}\text{Ca}^+$ has proved to be an excellent logic qubit, with stable hyperfine qubits allowing single-qubit gates and memory with errors $\sim 10^{-6}$ [36, 37], and state preparation, readout and two-qubit gates with errors $\lesssim 10^{-3}$ [26, 36, 38]. $^{88}\text{Sr}^+$ is superior for optical networking purposes due to its simple level structure and favourable wavelengths: high-rate, high-fidelity entanglement of ions in separate vacuum systems via a photonic link has recently been demonstrated with two $^{88}\text{Sr}^+$ ions [9].

Photon scattering sets a quasi-fundamental limit to the error for two-qubit gates driven by stimulated Raman transitions, and was the largest error contribution in the highest-fidelity two-qubit gates [26, 27]. To achieve a scattering error $\sim 10^{-4}$ requires several-THz detuning Δ of the Raman beams from resonance [39]. A laser tuned midway between the $^{43}\text{Ca}^+$ and $^{88}\text{Sr}^+$ S-P transitions yields a calculated scattering error of 2×10^{-4} , about a factor two lower than that in [26, 27]. The dominant technical errors are often due to motional and spin dephasing of the ions, which are smaller the faster the gate [26, 28]. To maintain a reasonable gate speed at THz detunings requires a beam power of a few tens of mW for

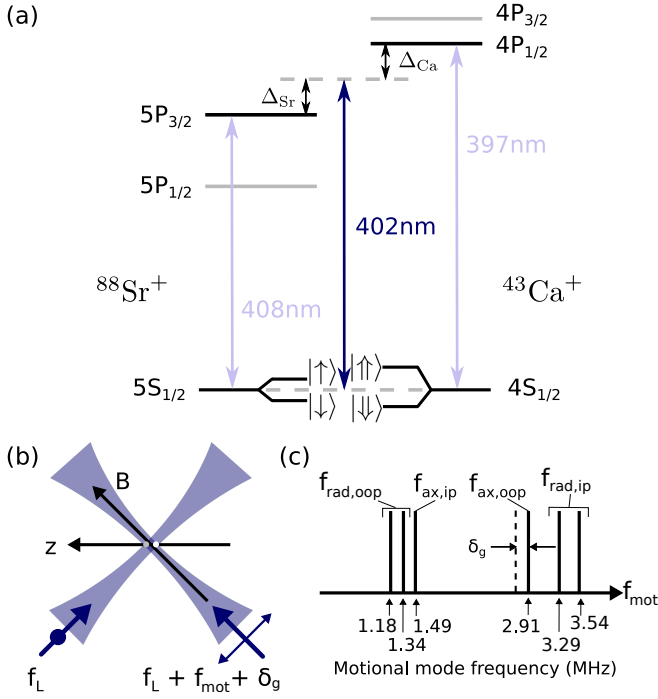


FIG. 1. (a) A single laser with wavelength $\lambda = c/f_L = 402 \text{ nm}$, detuned by $\Delta_{\text{Sr}} = +11.2 \text{ THz}$, $\Delta_{\text{Ca}} = -9.0 \text{ THz}$ from S-P transitions in $^{88}\text{Sr}^+$ and $^{43}\text{Ca}^+$, provides qubit-state-dependent forces on both ion species. The qubit states are $(|\downarrow\rangle, |\uparrow\rangle) = (5S_{1/2}^{-1/2}, 5S_{1/2}^{+1/2})$ in $^{88}\text{Sr}^+$ and $(|\psi\rangle, |\uparrow\rangle) = (4S_{1/2}^{4,+4}, 4S_{1/2}^{3,+3})$ in $^{43}\text{Ca}^+$. A static magnetic field $B = 146 \text{ G}$ gives qubit frequencies $f_{\downarrow} = 409 \text{ MHz}$ and $f_{\uparrow} = 2.874 \text{ GHz}$. The P_{1/2}-P_{3/2} fine-structure splittings are 24.03 THz in $^{88}\text{Sr}^+$ and 6.68 THz in $^{43}\text{Ca}^+$. (b) Both Raman beams are derived from a single frequency-doubled Ti:sapphire laser. The beatnote ($f_{\text{mot}} + \delta_g$) between the two beams is created by acousto-optic modulators. The differential wave vector $\Delta\mathbf{k}$ of the Raman beams is parallel to the trap axis \mathbf{z} , suppressing coupling to the radial modes of motion. (c) Values of (ax)ial and (rad)ial in-phase (ip) and out-of-phase (oop) normal mode frequencies.

30 μm spot sizes. We choose the Raman detuning to be roughly half-way between the nearest S-P transitions, at $\Delta_{\text{Ca}} = -9.0 \text{ THz}$ from the 397 nm transition in $^{43}\text{Ca}^+$, to couple similarly to both species. For our setup, this detuning also approximately minimizes the error due to motional heating during the gate [40].

The gate sequence is shown in Fig. 2a. The gate is implemented as two separate pulses enclosed by a spin-echo sequence, each pulse driving a closed-loop trajectory in motional phase space. This two-loop scheme reduces spin decoherence and cancels effects of the asymmetry of Ω_{\uparrow} and Ω_{\downarrow} in $^{43}\text{Ca}^+$ [32], where the Rabi frequencies Ω_{\uparrow} and Ω_{\downarrow} determine the strength of the light-shift on the two different qubit states. The phase of the second gate pulse is flipped by π in a 1st order Walsh modulation [41] to reduce sensitivity to mis-set parameters. In the $\sigma_z \otimes \sigma_z$ gate the phase of the single-qubit operations needs no fixed

relationship to the Raman beatnote phase [42]. Single-qubit operations are therefore driven independently using microwaves, with no phase coherence to the gate beams. The gate is performed on the axial out-of-phase motional mode, with a gate detuning of $\delta_g = -40 \text{ kHz}$ giving a gate time $t_g = 2/\delta_g = 49.2 \mu\text{s}$. The edges of the pulse are shaped with a $\sin^2(\pi t/2t_s)$ (Hann) window and a pulse-shaping time constant of $t_s = 2 \mu\text{s}$. The power in each Raman beam is 60 mW, in a spot size $\approx 30 \mu\text{m}$, giving $\Omega_{\downarrow}/2\pi = 180 \text{ kHz}$. For maximum gate efficiency, i.e. maximum two-qubit geometric phase acquired for a given carrier Rabi frequency, the $\sigma_z \otimes \sigma_z$ gate requires the ion spacing to be an integer or half-integer multiple of the Raman beam standing wave period $\lambda_z = 402 \text{ nm}/\sqrt{2}$. Low gate efficiency increases the sensitivity to errors. The ion spacing is $12.5\lambda_z = 3.57 \mu\text{m}$, leading to motional mode frequencies $f_{\text{ax,ip}} = 1.49 \text{ MHz}$ for the axial in-phase (ip) mode and $f_{\text{ax,oop}} = 2.91 \text{ MHz}$ for the axial out-of-phase (oop) mode (Fig. 1c). The radial oop mode frequencies are $f_{\text{rad,oop}} = 1.18 \text{ MHz}, 1.34 \text{ MHz}$, where several resonances need to be avoided: (i) $f_{\text{ax,oop}} \simeq 2f_{\text{rad,oop}}$, (ii) $f_{\text{ax,ip}} \simeq f_{\text{rad,oop}}$ and (iii) $2f_{\text{ax,ip}} \simeq f_{\text{ax,oop}}$. In these experiments the radial modes were not sub-Doppler cooled. For case (i), hot radial modes lead to large errors due to Kerr cross-coupling. For (ii), and if the Raman differential wave vector $\Delta\mathbf{k}$ is not orthogonal to the radial modes, additional errors can arise from radial mode excitation [28]. For (iii), certain gate detunings can lead to errors from higher harmonic excitation [24]. Therefore the trap frequencies and the sign of the gate detuning have to be chosen carefully to avoid these mode overlaps and resonances. The Lamb-Dicke parameters ($\eta_{\text{ip}}, \eta_{\text{oop}}$) are (0.090, 0.127) for $^{43}\text{Ca}^+$ and (0.124, 0.045) for $^{88}\text{Sr}^+$.

We characterize the error ϵ_G of the gate operation using three different methods: by measurement of the Bell state fidelity after a single gate operation using PST, and in longer sequences of gates using interleaved RBM and GST. For PST with a single gate operation we obtain $\epsilon_G = 2.0(1.0) \times 10^{-3}$ after correction for state preparation and measurement (SPAM) errors [21], averaged over 50 000 gate measurement shots taken over two separate days. The raw gate error before SPAM correction is $10.2(3) \times 10^{-3}$. For readout, the $^{88}\text{Sr}^+$ ion is shelved with a 674 nm pulse, which is sensitive to the ion temperature; for $^{43}\text{Ca}^+$ a 393 nm optical pumping process is used, which is far less temperature dependent [43]. As the ions are heated to Doppler temperature during fluorescence detection, we read out $^{88}\text{Sr}^+$ first. The average SPAM errors are $\bar{\epsilon}_{\text{Sr}} = 4.0(3) \times 10^{-3}$ for $^{88}\text{Sr}^+$ and $\bar{\epsilon}_{\text{Ca}} = 1.4(3) \times 10^{-3}$ for $^{43}\text{Ca}^+$, and the dominant uncertainty in ϵ_G arises from statistical uncertainty in $\bar{\epsilon}$.

RBM allows measurement of the gate error independent of SPAM errors, and also provides a measure of the gate error in the more computationally relevant context of long sequences of operations [30, 44, 45]. We implement an interleaved RBM protocol equivalent to that de-

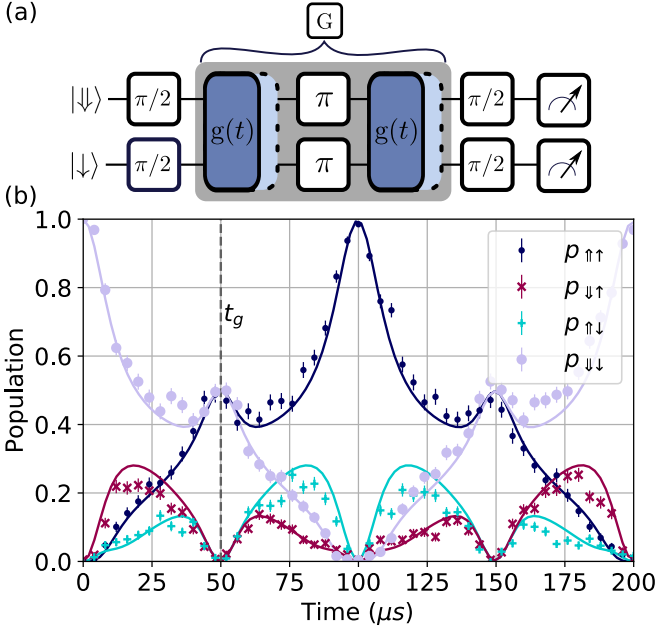


FIG. 2. (a) Schematic sequence of the $\sigma_z \otimes \sigma_z$ entangling gate. The gate G characterized in the RBM and GST measurements consists of two Raman pulses $g(t_{\text{loop}})$ separated by a “spin-echo” π -pulse on each qubit. For PST, G is bracketed by two $\pi/2$ -pulses, and followed by an additional $\pi/2$ analysis pulse (not shown), with phase $\phi = 45^\circ$ or 135° , to determine the parity contrast. (b) Gate dynamics measured with the sequence in (a). The asymmetry of the forces on $^{43}\text{Ca}^+$ and $^{88}\text{Sr}^+$ leads to the asymmetric evolution of the populations $p_{\downarrow\uparrow}$, $p_{\uparrow\downarrow}$. The abscissa gives the total duration of the two Raman pulses. Error bars are statistical.

scribed in [45], with the $\sigma_z \otimes \sigma_z$ operation as the “gate-under-test” G . The error per $\sigma_z \otimes \sigma_z$ gate ϵ_G is extracted by comparing the error rate ϵ_g of sequences of random Clifford operations to the error rate ϵ'_g of sequences which also include extra interleaved $\sigma_z \otimes \sigma_z$ gates, via [45]:

$$\epsilon_G = \frac{1}{\alpha_n} \left[1 - \frac{1 - \alpha_n \epsilon'_g}{1 - \alpha_n \epsilon_g} \right] \quad (1)$$

with depolarization probability $\alpha_n \epsilon$, where $\alpha_n = 2^n / (2^n - 1)$ and n is the number of qubits. Individually addressed single-qubit X and Y gates are achieved trivially through the use of different ion species, and single-qubit Z -rotations are implemented as software phase shifts. As both species participate in the gate operation, no sympathetic cooling is performed during the sequences. Experimental results are shown in Fig. 3. For each sequence length (up to 60 interleaved gates) we perform $N = 100$ shots of $k \simeq 100$ randomly-generated pairs of sequences. Each two-qubit Clifford operation contains on average 1.5 entangling operations as well as 7.7 single-qubit rotations, meaning that the longest sequences contain on average 151.5 entangling operations in total, and take 16 ms. Over these durations the increase in ion temperature and duty-cycle effects in am-

plifiers become non-negligible, leading to a slight increase in the error-per-gate for longer sequences (Fig. 3c). We measure $\epsilon_G = 2.9(7) \times 10^{-3}$ ($3.8(3) \times 10^{-3}$) from sequences with 20 (60) interleaved entangling gates-under-test, corresponding to sequences involving up to 51.5 (151.5) entangling gates. From the non-interleaved sequences alone, we can also extract the average error of an arbitrary two-qubit Clifford operation $\epsilon_g = 8.3(2) \times 10^{-3}$, consistent with the errors of its constituent operations.

To obtain a measure of the nature of the errors of different operations, in addition to their magnitude, GST can be employed [46]. We characterize the gate set $\{G, R_x(\pi/2), R_z(\pi/2)\}$, which contains 1026 gauge-independent parameters. To reduce the time necessary to estimate individual errors, we implement repetitions of shorter gate sequences, called germs, which are chosen to amplify specific errors [47]. A total of 62 germ sequences are used, each consisting of 1 to 5 operations. The germ sequences are optimized numerically, in turn amplifying sensitivity to a specific noise parameter with the minimum number of required operations. The germ sequences are surrounded by a preparation and a measurement fiducial, Fig. 4a. The fiducials serve to form complete sets of prepared states and measurement effects akin to process tomography. They are chosen from a set of 15 preparation and 10 measurement fiducials, each consisting of 1 to 4 operations per qubit. Operation sequences are constructed and analyzed from these sets using the pyGSTI package [48]. The error of the entangling gate G extracted from the results (Fig. 4) is $\epsilon_G = 6(3) \times 10^{-3}$ or a diamond norm distance $\|\cdot\|_\diamond = 0.03(1)$, where half of the error is due to coherent error sources.

The total numbers of qubit population measurements for results reported here are 250 000 for PST (including SPAM measurements), 132 000 for interleaved RBM and 386 000 for GST, where a single measurement takes 16 ms for PST, 16 – 32 ms for RBM and 16 – 23 ms for GST. The accuracy of both RBM and GST is limited by the increase of gate error with sequence length, which is not included as a fit parameter, and therefore reduces the quality of the fit. While PST is not affected by this systematic effect, it requires larger amounts of data than RBM to achieve equal statistical uncertainties, and can be subject to systematic error due to drifts in SPAM errors. GST provides information about the nature of gate errors that is essential for choosing and designing appropriate error correction algorithms [49]. However the reduction of the scaling efficiency of accuracy versus data set size due to the observed non-Markovianity (Fig. 4d), as well as the computational complexity of the analysis, make GST less convenient. In our regime of comparable gate and SPAM errors, RBM provides the most efficient accuracy for a given data acquisition time, and also reveals effects occurring in longer sequences.

Using different ion species puts more stringent requirements on several steps of calibration. Due to the dif-

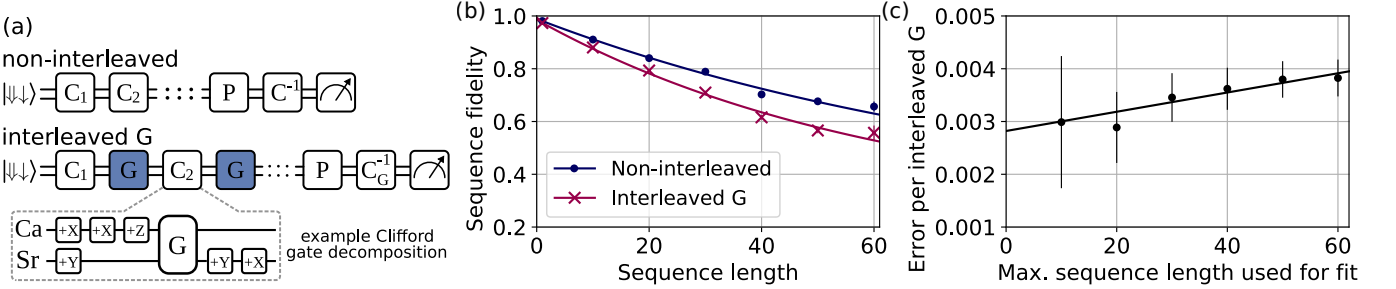


FIG. 3. Interleaved RBM: (a) Gate sequences. Each Clifford operation C_i is randomly chosen from the 11520 elements of the two-qubit Clifford group, generated by the single-qubit $\pi/2$ -rotations $\{\pm X, \pm Y, \pm Z\}$, and G . At the end of a sequence the inverse C^{-1} of all combined previous Clifford operations is applied so as to finish in an eigenstate of the measurement basis. A π - or identity pulse (P) is added at the end of the sequence to randomize the final eigenstate. In the interleaved sequence the entangling gate-under-test G is applied after each random Clifford operation. (b) Combined datasets of 660 randomized sequences, collected over two separate days, with up to 60 interleaved gates G . Each randomization is repeated 100 times to determine the sequence fidelity. Each datapoint corresponds to the mean of the sequence fidelities of all randomizations of a given sequence length. Error bars are statistical (standard error of the mean). (c) Error per interleaved gate G inferred from fitting the fidelity decay of the sequences in (b), as a function of the maximum sequence length used in the fit. The error-per-gate increases for longer sequences as certain error sources become more pronounced after longer durations. Error bars are inferred from parametric bootstrapping.

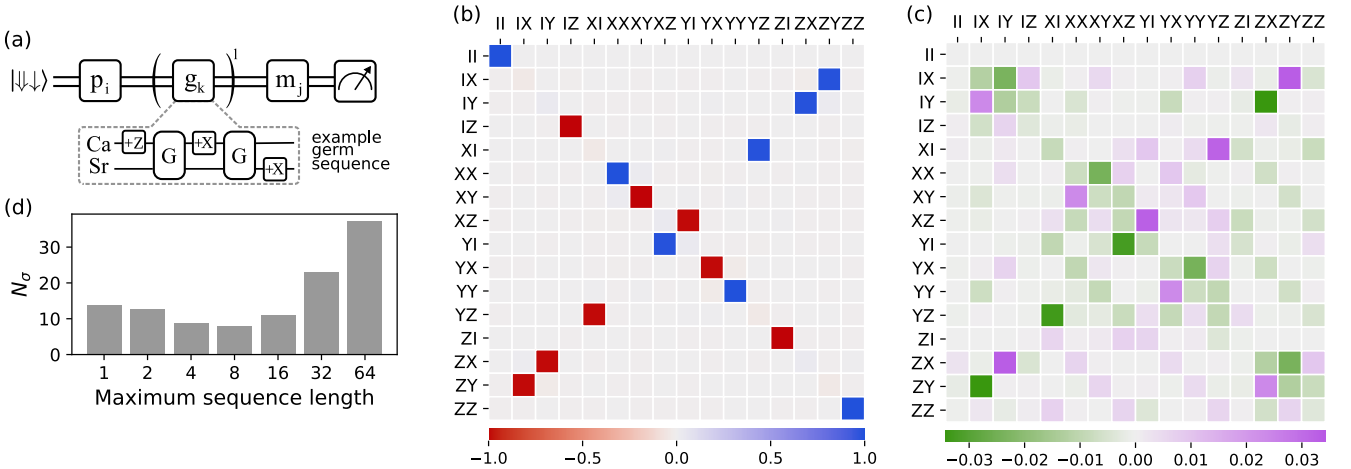


FIG. 4. Gate set tomography: (a) Structure of GST sequences. For each target sequence length $L = 1, 2, 4, \dots, 64$, each germ sequence g_k is repeated l times, such that the maximum number of operations is L , and is surrounded by combinations of preparation and measurement fiducials p_i and m_j . (b) Final maximum-likelihood estimate for the entangling gate under CPTP constraints, given as a superoperator \mathcal{G} in the Pauli-product basis. (c) Difference of the fit of the measured gate \mathcal{G} to the ideal gate \mathcal{G}_0 . Displayed is the error generator \mathbb{L} such that $\mathcal{G} = e^{\mathbb{L}} \mathcal{G}_0$. (d) Goodness-of-fit of the final estimate for data up to circuit length L , in units of standard deviations of the expected χ^2 distribution. A significant amount of non-Markovianity is present, presumably due to duty-cycle effects and motional heating.

ferent magnitude of the Raman detuning, the spin-orbit splitting, the Lamb-Dicke parameters and the matrix elements for $^{43}\text{Ca}^+$ and $^{88}\text{Sr}^+$, the effective Rabi frequency for the two ions is different. Therefore the net force on $|\uparrow\downarrow\rangle$ and $|\downarrow\uparrow\rangle$ is non-zero, and all four states $|\uparrow\downarrow\rangle$, $|\downarrow\uparrow\rangle$, $|\uparrow\uparrow\rangle$ and $|\downarrow\downarrow\rangle$ are motionally excited by the light-shift force. This means that some of the acquired geometric phase gives rise to a global phase $I \otimes I$ instead of the desired two-qubit phase $\sigma_z \otimes \sigma_z$. Therefore the

total Rabi frequency has to be increased and the maximum excursion in phase space becomes larger. This increases the sensitivity to errors due to imperfect closure of loops in motional phase space, to heating errors, and to photon scattering errors, compared with more efficient single-species gates. Due to the mass-dependence of the rf pseudo-potential, mixed-species crystals tilt off the trap z -axis if there are stray electric fields in the trap that displace the ions radially [35]. This leads to errors,

for example by increasing the coupling of the gate lasers to radial modes. The gate error increases quadratically with increasing magnitude of an external field. For a field strength of 10 V/m we observe an error of 7×10^{-2} . This is considerably larger than the error expected from changes in Lamb-Dicke parameters. Trap compensation therefore has to be adjusted more carefully than for a single-species crystal. To mitigate the effects of inhomogeneities and field gradients in the trap [35], the ion order is kept constant [33, 50].

Estimated contributions to the Ca–Sr gate error are: 2×10^{-4} from Raman and Rayleigh photon scattering, 4×10^{-4} due to ion heating (heating rate ≈ 30 quanta/s for the Ca–Sr axial out-of-phase mode), 1×10^{-4} due to coupling to spectator modes, $< 1 \times 10^{-4}$ due to spin dephasing, and $\lesssim 2 \times 10^{-4}$ from Kerr cross-coupling (assuming coupling similar to a single-species crystal). The mean error of the single-qubit microwave operations used for the spin-echo sequence enclosing the gate pulses was determined independently using single-qubit RBM, and is $4.3(2) \times 10^{-4}$ for a $\pi/2$ -pulse.

In summary, we have performed a mixed-element entangling gate on $^{43}\text{Ca}^+$ and $^{88}\text{Sr}^+$ ground-level qubits using a light-shift gate previously used for same-element gates. We have characterized the gate operation using three different methods which yield consistent results, and give a gate fidelity comparable to that of the best single-species gates. The gate mechanism requires one pair of beams from a single, visible-wavelength c.w. laser, making it promising for use in scalable quantum computing architectures.

VMS is a Junior Research Fellow at Christ Church College, Oxford. SRW was funded by the U.K. National Physical Laboratory, KT by the U.K. Defence Science and Technology Laboratory. CJB is supported by a UKRI FL Fellowship, and is a Director of Oxford Ionics Ltd. This work was funded by the U.K. EPSRC “Networked Quantum Information Technology” and “Quantum Computing and Simulation” Hubs, and by the E.U. Quantum Technology Flagship project AQTION (820495).

CJB and DML conceived the experiment. KT, VMS, ACH, CJB and SRW built the apparatus. VMS, CJB, ACH and KT designed the experiment. ACH, VMS and DPN took and analyzed the data and produced the figures. VMS, DML and ACH wrote the manuscript, which all authors discussed.

[†] These authors contributed equally

^{*} vera.schafer@physics.ox.ac.uk

[1] D. J. Wineland, C. Monroe, W. M. Itano, D. Leibfried, B. E. King, and D. M. Meekhof, Experimental issues in coherent quantum-state manipulation of trapped atomic ions, *J. Res. Natl. Inst. Stand. Technol.* **103**, 259 (1998).

[2] W. Pfaff, T. H. Taminiau, L. Robledo, H. Bernien, M. Markham, D. J. Twitchen, and R. Hanson, Demonstration of entanglement-by-measurement of solid-state qubits, *Nat. Phys.* **9**, 29 (2013).

[3] A. Wallraff, D. I. Schuster, A. Blais, L. Frunzio, R. S. Huang, J. Majer, S. Kumar, S. M. Girvin, and R. J. Schoelkopf, Strong coupling of a single photon to a superconducting qubit using circuit quantum electrodynamics, *Nature* **431**, 162 (2004).

[4] S. Ritter, C. Nölleke, C. Hahn, A. Reiserer, A. Neuzner, M. Uphoff, M. Mücke, E. Figueroa, J. Bochmann, and G. Rempe, An elementary quantum network of single atoms in optical cavities, *Nature* **484**, 195 (2012).

[5] D. Hucul, I. V. Inlek, G. Vittorini, C. Crocker, S. Debnath, S. M. Clark, and C. Monroe, Modular entanglement of atomic qubits using photons and phonons, *Nat. Phys.* **11**, 37 (2015).

[6] R. Nigmatullin, C. J. Ballance, N. de Beaudrap, and S. C. Benjamin, Minimally complex ion traps as modules for quantum communication and computing, *New J. Phys.* **18**, 103028 (2016).

[7] X. Mi, J. V. Cady, D. M. Zajac, P. W. Deelman, and J. R. Petta, Strong coupling of a single electron in silicon to a microwave photon, *Science (80-.)* **355**, 156 (2017).

[8] P. C. Humphreys, N. Kalb, J. P. J. Morits, R. N. Schouten, R. F. L. Vermeulen, D. J. Twitchen, M. Markham, and R. Hanson, Deterministic delivery of remote entanglement on a quantum network, *Nature* **558**, 268 (2018).

[9] L. J. Stephenson, D. P. Nadlinger, B. C. Nichol, S. An, P. Drmota, T. G. Ballance, K. Thirumalai, J. F. Goodwin, D. M. Lucas, and C. J. Ballance, High-rate, high-fidelity entanglement of qubits across an elementary quantum network, *Phys. Rev. Lett.* **124**, 110501 (2020).

[10] H. M. Meyer, R. Stockill, M. Steiner, C. Le Gall, C. Matthiesen, E. Clarke, A. Ludwig, J. Reichel, M. Atatüre, and M. Köhl, Direct photonic coupling of a semiconductor quantum dot and a trapped ion, *Phys. Rev. Lett.* **114**, 123001 (2015).

[11] K. D. Petersson, L. W. McFaul, M. D. Schroer, M. Jung, J. M. Taylor, A. A. Houck, and J. R. Petta, Circuit quantum electrodynamics with a spin qubit, *Nature* **490**, 380 (2012).

[12] D. Marcos, M. Wubs, J. M. Taylor, R. Aguado, M. D. Lukin, and A. S. Sørensen, Coupling nitrogen-vacancy centers in diamond to superconducting flux qubits, *Phys. Rev. Lett.* **105**, 210501 (2010).

[13] P. O. Schmidt, T. Rosenband, C. Langer, W. M. Itano, J. C. Bergquist, and D. J. Wineland, Spectroscopy using quantum logic, *Science (80-.)* **309**, 749 (2005).

[14] C. W. Chou, C. Kurz, D. B. Hume, P. N. Plessow, D. R. Leibrandt, and D. Leibfried, Preparation and coherent manipulation of pure quantum states of a single molecular ion, *Nature* **545**, 203 (2017).

[15] S. M. Brewer, J. S. Chen, A. M. Hankin, E. R. Clements, C. W. Chou, D. J. Wineland, D. B. Hume, and D. R. Leibrandt, $^{27}\text{Al}^+$ quantum-logic clock with a systematic uncertainty below 10^{-18} , *Phys. Rev. Lett.* **123**, 033201 (2019).

[16] L. Schmöger, O. O. Versolato, M. Schwarz, M. Kohnen, A. Windberger, B. Piest, S. Feuchtenbeiner, J. Pedregosa-Gutierrez, T. Leopold, P. Micke, A. K.

Hansen, T. M. Baumann, M. Drewsen, J. Ullrich, P. O. Schmidt, and J. R. C. López-Urrutia, Coulomb crystallization of highly charged ions, *Science* (80- .). **347**, 1233 (2015).

[17] C. Smorra, K. Blaum, L. Bojtar, M. Borchert, K. A. Franke, T. Higuchi, N. Leefer, H. Nagahama, Y. Matsuda, A. Mooser, M. Niemann, C. Ospelkaus, W. Quint, G. Schneider, S. Sellner, T. Tanaka, S. Van Gorp, J. Walz, Y. Yamazaki, and S. Ulmer, BASE The Baryon Antibaryon Symmetry Experiment, *Eur. Phys. J. Spec. Top.* **224**, 3055 (2015).

[18] M. D. Barrett, B. DeMarco, T. Schaetz, V. Meyer, D. Leibfried, J. Britton, J. Chiaverini, W. M. Itano, B. Jelenković, J. D. Jost, C. Langer, T. Rosenband, and D. J. Wineland, Sympathetic cooling of ${}^9\text{Be}^+$ and ${}^{24}\text{Mg}^+$ for quantum logic, *Phys. Rev. A* **68**, 042302 (2003).

[19] J. P. Home, M. J. McDonnell, D. J. Szwer, B. C. Keitch, D. M. Lucas, D. N. Stacey, and A. M. Steane, Memory coherence of a sympathetically cooled trapped-ion qubit, *Phys. Rev. A* **79**, 050305 (2009).

[20] I. V. Inlek, C. Crocker, M. Lichtman, K. Sosnova, and C. Monroe, Multispecies trapped-ion node for quantum networking, *Phys. Rev. Lett.* **118**, 250502 (2017).

[21] C. J. Ballance, V. M. Schäfer, J. P. Home, D. J. Szwer, S. C. Webster, D. T. C. Allcock, N. M. Linke, T. P. Harty, D. P. L. Aude Craik, D. N. Stacey, A. M. Steane, and D. M. Lucas, Hybrid quantum logic and a test of Bell's inequality using two different atomic isotopes, *Nature* **528**, 384 (2015).

[22] T. R. Tan, J. P. Gaebler, Y. Lin, Y. Wan, R. Bowler, D. Leibfried, and D. J. Wineland, Multi-element logic gates for trapped-ion qubits, *Nature* **528**, 380 (2015).

[23] V. Negnevitsky, M. Marinelli, K. K. Mehta, H. Y. Lo, C. Flühmann, and J. P. Home, Repeated multi-qubit readout and feedback with a mixed-species trapped-ion register, *Nature* **563**, 527 (2018).

[24] C. D. Bruzewicz, R. McConnell, J. Stuart, J. M. Sage, and J. Chiaverini, Dual-species, multi-qubit logic primitives for Ca^+/Sr^+ trapped-ion crystals, *npj Quantum Inf.* **5**, 102 (2019).

[25] Y. Wan, D. Kienzler, S. D. Erickson, K. H. Mayer, T. R. Tan, J. J. Wu, H. M. Vasconcelos, S. Glancy, E. Knill, D. J. Wineland, A. C. Wilson, and D. Leibfried, Quantum gate teleportation between separated qubits in a trapped-ion processor, *Science* (80- .). **364**, 875 (2019).

[26] C. J. Ballance, T. P. Harty, N. M. Linke, M. A. Sepiol, and D. M. Lucas, High-fidelity quantum logic gates using trapped-ion hyperfine qubits, *Phys. Rev. Lett.* **117**, 060504 (2016).

[27] J. P. Gaebler, T. R. Tan, Y. Lin, Y. Wan, R. Bowler, A. C. Keith, S. Glancy, K. Coakley, E. Knill, D. Leibfried, and D. J. Wineland, High-fidelity universal gate set for ${}^9\text{Be}^+$ ion qubits, *Phys. Rev. Lett.* **117**, 060505 (2016).

[28] V. M. Schäfer, C. J. Ballance, K. Thirumalai, L. J. Stephenson, T. G. Ballance, A. M. Steane, and D. M. Lucas, Fast quantum logic gates with trapped-ion qubits, *Nature* **555**, 75 (2017).

[29] A. Erhard, J. J. Wallman, L. Postler, M. Meth, R. Stricker, E. A. Martinez, P. Schindler, T. Monz, J. Emerson, and R. Blatt, Characterizing large-scale quantum computers via cycle benchmarking, *Nat. Commun.* **10**, 5347 (2019).

[30] C. H. Baldwin, B. J. Bjork, J. P. Gaebler, D. Hayes, and D. Stack, Subspace benchmarking high-fidelity entangling operations with trapped ions, *Phys. Rev. Res.* **2**, 013317 (2020).

[31] D. Leibfried, B. DeMarco, V. Meyer, D. Lucas, M. Barrett, J. Britton, W. M. Itano, B. Jelenković, C. Langer, T. Rosenband, and D. J. Wineland, Experimental demonstration of a robust, high-fidelity geometric two ion-qubit phase gate, *Nature* **422**, 412 (2003).

[32] C. J. Ballance, *High-fidelity quantum logic in Ca^+* , Ph.D. thesis, University of Oxford (2014).

[33] V. M. Schäfer, *Fast gates and mixed-species entanglement with trapped ions*, Ph.D. thesis, University of Oxford (2018).

[34] G. Morigi and H. Walther, Two-species Coulomb chains for quantum information, *Eur. Phys. J. D* **13**, 261 (2001).

[35] J. P. Home, Quantum science and metrology with mixed-species ion chains, *Adv. At. Mol. Opt. Phys.* **62**, 231 (2013).

[36] T. P. Harty, D. T. C. Allcock, C. J. Ballance, L. Guidoni, H. A. Janacek, N. M. Linke, D. N. Stacey, and D. M. Lucas, High-fidelity preparation, gates, memory, and readout of a trapped-ion quantum bit, *Phys. Rev. Lett.* **113**, 220501 (2014).

[37] M. A. Sepiol, A. C. Hughes, J. E. Tarlton, D. P. Nadlinger, T. G. Ballance, C. J. Ballance, T. P. Harty, A. M. Steane, J. F. Goodwin, and D. M. Lucas, Probing qubit memory errors at the part-per-million level, *Phys. Rev. Lett.* **123**, 110503 (2019).

[38] T. P. Harty, M. A. Sepiol, D. T. C. Allcock, C. J. Ballance, J. E. Tarlton, and D. M. Lucas, High-fidelity trapped-ion quantum logic using near-field microwaves, *Phys. Rev. Lett.* **117**, 140501 (2016).

[39] R. Ozeri, W. M. Itano, R. Blakestad, J. Britton, J. Chiaverini, J. D. Jost, C. Langer, D. Leibfried, R. Reichle, S. Seidelin, J. H. Wesenberg, and D. J. Wineland, Errors in trapped-ion quantum gates due to spontaneous photon scattering, *Phys. Rev. A* **75**, 042329 (2007).

[40] manuscript in preparation.

[41] D. Hayes, S. M. Clark, S. Debnath, D. Hucul, I. V. Inlek, K. W. Lee, Q. Quraishi, and C. Monroe, Coherent error suppression in multiqubit entangling gates, *Phys. Rev. Lett.* **109**, 020503 (2012).

[42] P. J. Lee, K. A. Brickman, L. Deslauriers, P. C. Haljan, L. M. Duan, and C. Monroe, Phase control of trapped ion quantum gates, *J. Opt. B* **7**, 371 (2005).

[43] A. Myerson, D. Szwer, S. Webster, D. Allcock, M. Curtis, G. Imreh, J. Sherman, D. Stacey, A. Steane, and D. Lucas, High-fidelity readout of trapped-ion qubits, *Phys. Rev. Lett.* **100**, 200502 (2008).

[44] E. Knill, D. Leibfried, R. Reichle, J. Britton, R. B. Blakestad, J. D. Jost, C. Langer, R. Ozeri, S. Seidelin, and D. J. Wineland, Randomized benchmarking of quantum gates, *Phys. Rev. A* **77**, 012307 (2008).

[45] J. P. Gaebler, A. M. Meier, T. R. Tan, R. Bowler, Y. Lin, D. Hanneke, J. D. Jost, J. P. Home, E. Knill, D. Leibfried, and D. J. Wineland, Randomized Benchmarking of Multiqubit Gates, *Phys. Rev. Lett.* **108**, 260503 (2012).

[46] R. Blume-Kohout, J. K. Gamble, E. Nielsen, J. Mizrahi, J. D. Sterk, and P. Maunz, Robust, self-consistent, closed-form tomography of quantum logic gates on a trapped ion qubit, *arXiv* , 1310.4492 (2013).

[47] R. Blume-Kohout, J. K. Gamble, E. Nielsen, K. Rudinger, J. Mizrahi, K. Fortier, and P. Maunz, Demonstration of qubit operations below a rigorous fault tolerance threshold with gate set tomography, *Nat.*

Commun. **8**, 14485 (2017).

[48] E. Nielsen, K. Rudinger, J. K. Gamble, and R. Blume-Kohout, pyGSTi: A python implementation of gate set tomography (2016).

[49] D. Gottesman, An introduction to quantum error correction and fault-tolerant quantum computation, Proc. Symp. Appl. Math. **68**, 13 (2010).

[50] J. P. Home, D. Hanneke, J. D. Jost, D. Leibfried, and D. J. Wineland, Normal modes of trapped ions in the presence of anharmonic trap potentials, New J. Phys. **13**, 073026 (2011).